A covalent molecular design enabling efficient CO_2 reduction in strong acids

Zhang, Qiang; Musgrave III, Charles B.; Song, Yun; Su, Jianjun; Huang, Libei; Cheng, Le; Li, Geng; Liu, Yong; Xin, Yinger; Hu, Qiushi; Ye, Ge; Shen, Hanchen; Wang, Xue; Tang, Ben Zhong; Goddard III, William A.; Ye, Ruquan

Published in:
Nature Synthesis

Online published: 25/06/2024

Document Version:
Post-print, also known as Accepted Author Manuscript, Peer-reviewed or Author Final version

Publication record in CityU Scholars:
Go to record

Published version (DOI):
10.1038/s44160-024-00588-4

Publication details:
Zhang, Q., Musgrave III, C. B., Song, Y., Su, J., Huang, L., Cheng, L., Li, G., Liu, Y., Xin, Y., Hu, Q., Ye, G., Shen, H., Wang, X., Tang, B. Z., Goddard III, W. A., & Ye, R. (2024). A covalent molecular design enabling efficient CO_2 reduction in strong acids. *Nature Synthesis*. Advance online publication. https://doi.org/10.1038/s44160-024-00588-4

A covalent molecular design enabling efficient CO_2 reduction in strong acids

Qiang Zhang[1,2#], Charles B. Musgrave III[3#], Yun Song[1,2], Jianjun Su[1,2], Libei Huang[1,2], Le Cheng[1,2], Geng Li[1,2], Yong Liu[1,2], Yinger Xin[1,2], Qiushi Hu[1,2], Ge Ye[1,2], Hanchen Shen[4], Xue Wang[5], Ben Zhong Tang[4*], William A. Goddard III[3*] and Ruquan Ye[1,2*]

[1]*Department of Chemistry, State Key Laboratory of Marine Pollution, City University of Hong Kong, Hong Kong 999077, P. R. China*

[2]*City University of Hong Kong Shenzhen Research Institute, Shenzhen 518000, P. R. China*

[3]*Materials and Process Simulation Center, California Institute of Technology, Pasadena, CA, USA.*

[4]*School of Science and Engineering, Shenzhen Institute of Aggregate Science and Technology, The Chinese University of Hong Kong, Shenzhen (CUHK-Shenzhen), Guangdong 518172, China.*

[5]*School of Energy and Environment, City University of Hong Kong, Hong Kong, 999077, China*

[#]*Equal contribution*

[*] *Corresponding authors:*

Ben Zhong Tang: tangbenz@cuhk.edu.cn; ORCID: 0000-0002-0293-964X

William A. Goddard III: wag@caltech.edu; ORCID:0000-0003-0097-5716

Ruquan Ye: ruquanye@cityu.edu.hk; ORCID: 0000-0002-2543-9090

Abstract

Molecular complexes constitute an important class of catalysts for the carbon dioxide reduction reaction (CO_2RR). However, selective CO_2RR in strong acids remains challenging due to the competition with the hydrogen evolution reaction (HER). Peripheral functionalization is effective in tailoring the intrinsic activity of molecular catalysts, mostly attributed to the inductive effect or to stabilization of particular reaction intermediates. Here we report that peripheral functionalization of immobilized molecular complexes with quaternary ammonium groups can regulate the catalytic activity by precisely and stably tuning the kinetics and mass transport surrounding active sites, enabling high-performance CO_2RR in strong acids. The positive charges and hydrophobic alkylammonium groups affect the migration of water and hydronium in the double layer while the covalent cationic configuration stabilizes interfaces, combining to inhibit HER over extended potential windows. The effectiveness of our strategy is evidenced

by testing of various metallophthalocyanines and metalloporphyrins, showing significantly improved acidic CO_2RR compared to the pristine molecules. For example, dodecyl ammonium-functionalized cobalt phthalocyanine and tin porphyrin suppress the hydrogen Faradaic efficiency to <10% in pH≈0.5 media, while providing a single-pass conversion efficiency up to ~85%. The selectivity can be maintained at 90% even in Li^+ solutions, which often exhibit poor proton shielding. Our study underscores the role of second-sphere structure for selective molecular electrochemistry.

Keywords: strong acids; CO_2 reduction; molecular electrocatalysis; carbon utilization; local microenvironment

Introduction

The electrocatalytic CO_2RR for production of valuable chemicals and fuels is widely studied as a potential solution for renewable energy storage and carbon neutralization[1]. Alkaline and neutral electrolytes are predominantly used in current electrolysis systems[2-6] because an alkaline environment surrounding the electrode surface aides CO_2 activation while suppressing the competitive HER[7-10]. However, practical applications of alkaline/neutral system are hampered by several shortcomings. Firstly, over 75% of the input CO_2 is consumed by reaction with hydroxide to form carbonate or bicarbonate, leading to carbon loss and crossing of liquid products over the anion exchange membrane (AEM)[11-15]. Secondly, a continuous input of CO_2 reduces the pH of the electrolyte, leading to poor catalyst and membrane stability[16]. The electrolyte must be refreshed periodically as a consequence, especially in alkaline medium[17]. One solution to these problems is to perform CO_2RR in acidic conditions. In acidic solutions (pH<3.75), the CO_3^{2-} or HCO_3^- generated convert back to CO_2 after it diffuses from the electrode surface to the bulk acidic electrolyte[18,19]. Furthermore, using a proton exchange membrane (PEM) in acidic CO_2RR prevents migration of liquid products to the anode, which avoids product loss[20]. Acidic CO_2RR also permits the use of proton-exchange membrane electrolyzers, which show higher ionic conductivity than competing AEM designs[21, 22]. However, the high hydronium ion concentration in acid promotes HER, leading to lower Faradaic efficiency (FE) of CO_2RR products[23,24]. HER suppression is therefore challenging for acidic CO_2RR, yet imperative for future applications.

Modulation of local environments using concentrated alkali metal solutions has been shown to mitigate competing HER in acid. Several metal-based catalysts, such as Au[16,25], Ag[26], Bi[19], Cu-Bi[27], Ni_5@NCN[28], and Cu/PFSA[29], have demonstrated high carbon utilization efficiency. It was proposed that the alkali cations under a reductive potential will form a cationic shield in the double layer, thus retarding hydronium migration[16]. However, a high concentration of alkali metal in solution can easily lead to salt precipitation during long-term electrolysis. In addition, the CO_2RR FE is maintained within only a small potential window while HER gradually dominates the overall reaction at high current densities[16]. This likely arises due to the strong coulomb attraction to the hydronium at more negative potential. Another possible route for achieving acidic CO_2RR is the use of organic materials to modify the interface environment. For example, polymer coatings on metal catalysts have been reported to reduce HER activity[30-32]. However, the addition of an overlayer increases charge transfer resistance and impedes mass transport in the diffusion layer, thus leading to higher resistivity and increased energy loss in practical operation[30]. The addition of organic cations in solution also affects the CO_2RR performance, but this works only for certain metal catalysts and the mechanism remains unclear[33].

To mitigate the limitations of concentrated alkali electrolyte and overlayer coatings, an alternative strategy for acidic CO_2RR is direct covalent modulation of the local environment surrounding the catalytic active sites. Covalently immobilizing functionalities can form a more stable local field than mobile cations in solution. In addition, peripheral functionalization mostly affects the mass transport in the double layer with negligible impact on the diffusion layer, thus alleviating resistivity issues. Among numerous potential catalysts, molecular complexes[34-37] provide a promising platform by virtue of their well-defined active sites and tailorable catalytic activity via peripheral functionalization with various substituents[38,39]. These substituents with different propensities change the electronic structure of the metal centers, thus affecting their intrinsic catalytic activity. Here we show that in addition to this electronic structure rearrangement, covalent functionalization of molecular catalysts with quaternary ammonium groups in the second sphere can also effectively change the mass transport within the double layer, thus providing a general approach to improve the extrinsic activity of molecular catalysts. We show that the positive charges of quaternary ammoniums repel hydroniums via coulomb repulsion, thus decreasing hydronium reduction activity. In addition, we establish that ammonium groups with longer alkyl chains can further deactivate the water reduction activity due to weakened van der Waals interactions. Indeed, rotating disk electrode (RDE)

voltammetry shows that cationic alkyl groups significantly reduce the HER current from 1.14 A cm^{-2} down to 0.14 A cm^{-2} after alkylation. Combining the two interactions, we achieve efficient CO_2RR in strong acid (pH≈0.5) for various molecular catalysts functionalized with quaternary ammoniums, obtaining <10% FE for hydrogen with single-pass conversion efficiency up to ~85%. Our new strategy may be universal to other organometallic catalysts for efficient acidic CO_2RR, including other molecular catalysts and their polymeric forms.

Synthesis and characterization of CoTAAPc@CNT-n

Fig. 1 illustrates several CO_2RR interfaces reported in the literature. In the conventional interface, the electrocatalysts are in direct contact with the hydrogen ions in the acidic electrolyte, leading to low ionic resistivity and dominant HER (Fig. 1a)[23,24,40]. Several researchers have used high concentrations of alkali cations to suppress hydronium reduction, demonstrating low HER in strongly acidic media (Fig. 1b)[19,29,41,42]. However, the selectivity could be maintained only in a limited potential window, with salt precipitation occurring during long-term electrolysis, which precludes practical application. Some researchers also introduced hydrophobic or ionic polymers to suppress HER (Fig. 1c)[43,44]. These latter methods displayed good potential windows for selective CO_2RR, but the overlayer coatings decrease mass transport in the diffusion layer; the high impedance to ion/water conduction unfavorably increases energy loss during electrolysis. In our current study, we introduce quaternary ammonium groups to the molecular catalysts for selective, acidic CO_2RR. Because of the hydrophobic alkyl chains and the cationic ammonium groups, HER is greatly suppressed in acidic electrolyte. In addition, unlike the alkali metals in electrolyte, the covalently bonded cations are immobile, which forms stable local environments, enabling a wider working potential window. This covalent feature also minimizes the interference of mass transport in the diffusion layer (Fig. 1d), as compared to the overlayer coating methods.

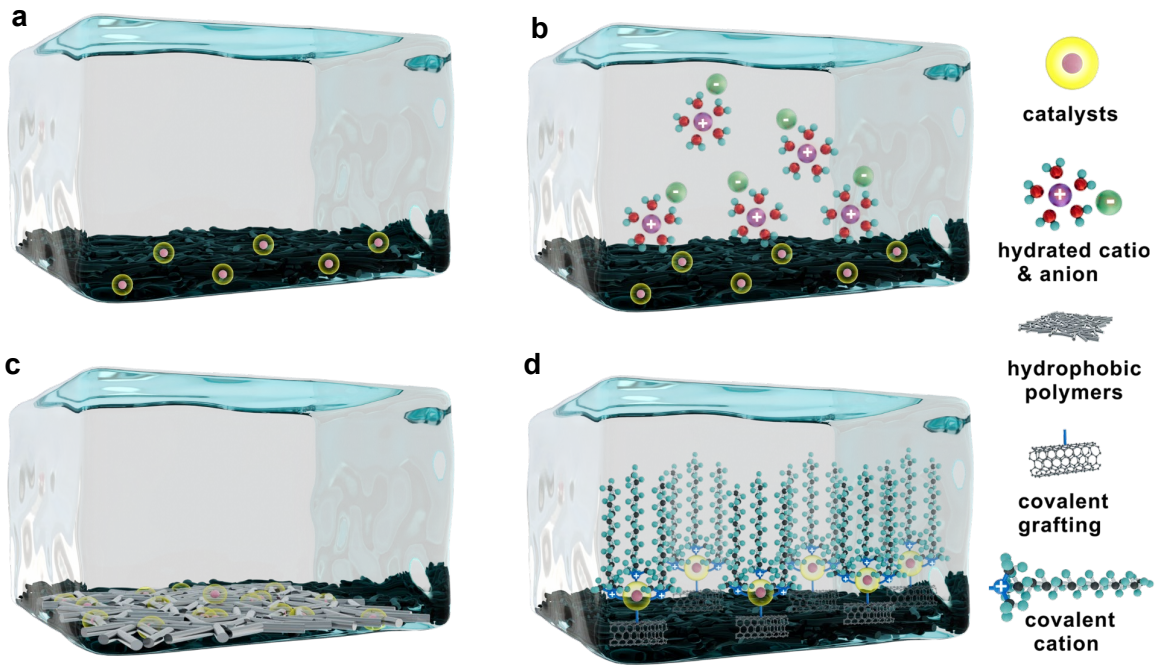

Fig. 1 Schematic of electrochemical CO_2RR in acidic electrolytes with various strategies. a, Conventional interface between catalysts and acidic electrolytes. **b**, Strategy using concentrated alkali cations. **c**, Strategy using polymer coatings. **d**, Our strategy using peripheral functionalization with long-alkyl-chain quaternary ammonium groups.

We took cobalt tetraaminophthalocyanine (CoTAPc) as a typical example to demonstrate our strategy for synthesizing molecular catalysts with various quaternary ammonium groups. The synthesis of cobalt (II) tetra alkylated ammonium phthalocyanine on CNT (CoTAAPc@CNT-n, where n denotes the length of alkyl chains in the ammonium groups) involved a three-step process (Fig. 2a and Method). First, CoTAPc@CNT was prepared by a diazonium reaction between CoTAPc and CNT. This covalent immobilization can resolve the catalysts' leaching issues, particularly for ionic molecules[6]. Iodoalkane was then used to introduce various alkyl chains to the ammonium groups. We found that long-chain iodoalkane has a low reactivity towards complete quaternization. Thus, we took an additional methylation step to form the ammonium groups, affording three types of CoTAAPc@CNT: CoTAAPc@CNT-1, CoTAAPc@CNT-6, CoTAAPc@CNT-12.

We first used Raman spectra to show the successful formation of the hybrid materials (Fig. 2b). The pristine CNT has two signature peaks at 1355 and 1579 cm^{-1}, corresponding to the D and G bands[45]. These

molecule-modified CNTs exhibit some fine signals from molecular monomers at 1000-1500 cm^{-1} (Supplementary Fig. 1). The ratio of the D to G peak intensity (I_D/I_G) indicates the degree of disorder of the carbon materials. The molecule-modified CNT samples have a higher I_D/I_G value (0.23-0.24) than the pristine CNT (0.20), which likely arises from disturbances of the surface lattice after the covalent grafting[46]. Transmission electron microscopy (TEM) reveals that, considering CoTAAPc@CNT-12 for example, there is a smooth surface morphology similar to pristine CNT without obvious aggregation of molecular monomers (Fig. 2c). The Z-contrast high-angle annular dark field high resolution aberration-corrected scanning transmission electron microscopy (HAADF-STEM) image of CoTAAPc@CNT-12 shows highly dispersed Co sites on the CNT surfaces, as indicated by the circled bright spots (Fig. 2d). The energy dispersive X-ray spectroscopy (EDS) mappings also show a uniform distribution of N and Co elements alongside the CNT (Fig. 2e). Inductively coupled plasma mass spectrometry (ICP-MS) reveals a similar Co concentration in CoTAPc@CNT and CoTAAPc@CNT-n at approximately 0.63 wt.%.

We then used Fourier transform infrared (FT-IR) spectroscopy and X-ray photoelectron spectroscopy (XPS) to investigate the catalyst structures (Supplementary Fig. 2 and Fig. 2f, g). Since the FT-IR signal of CoTAAPc@CNT-n is interfered significantly by the CNT background (Supplementary Fig. 2), we synthesized the molecular monomers without CNT substrates (CoTAAPc-n) for structural validation. After quaternization, the amine vibrational peaks at 3339 and 3210 cm^{-1} of CoTAPc disappeared in CoTAAPc-n. At the same time, new peaks at 945 and 1484 cm^{-1} emerge, corresponding to new C-N stretching and -CH_2 bending of -N^+-CH_2 groups[47,48]. Notably, extra characteristic C-H vibration peaks at approximately 2900 cm^{-1} are also present in CoTAAPc-n, suggesting successful introduction of alkyl chains (Supplementary Fig. 2)[30]. Similar structural transitions are also observed in XPS tests for CoTAAPc@CNT-n. CoTAPc@CNT shows two N 1s peaks at 398.68 and 400.18 eV from phthalocyanine entities and amine, respectively. After quaternization, the CoTAAPc@CNT-n displays new peaks at ~402.00 eV, corresponding to the quaternary ammonium nitrogen[30,49,50]. The Co 2p spectra shows the valence state of coordinated cobalt atoms. The binding energies of Co $2p_{3/2}$ and Co $2p_{1/2}$ for CoTAPc@CNT are at 780.39 and 796.01 eV, which shift to lower binding energies (779.78 and 795.49 eV, respectively) for CoTAAPc@CNT-12[6,49]. This variation is due to the transformation of electron-donating amino groups into electron-withdrawing quaternary ammonium groups[51,52]. The ^1H nuclear magnetic resonance (NMR) spectra of CoTAAPc-n also shows a strong signal at 3.04 ppm from the alkyl chain (Supplementary Fig.

3)[53]. In the UV-visible spectra, the Q band absorbance peaks are blue-shifted to lower wavelength after quaternization, which we attribute to the strong electron-withdrawing effect of the quaternary ammonium groups (Supplementary Fig. 4)[54]. After covalently immobilizing molecular monomers on the CNTs, their positively charged structures were further verified by zeta potential analysis (Fig. 2h). The aqueous dispersions of CoTAPc@CNT, CoTAAPc@CNT-1, CoTAAPc@CNT-6, and CoTAAPc@CNT-12 show zeta potentials of -43.7, 11.8, 10.7 and 10.8 mV, respectively. Moreover, the above characterizations confirm our successful synthesis of positively charged catalysts with alkyl chains of varying length.

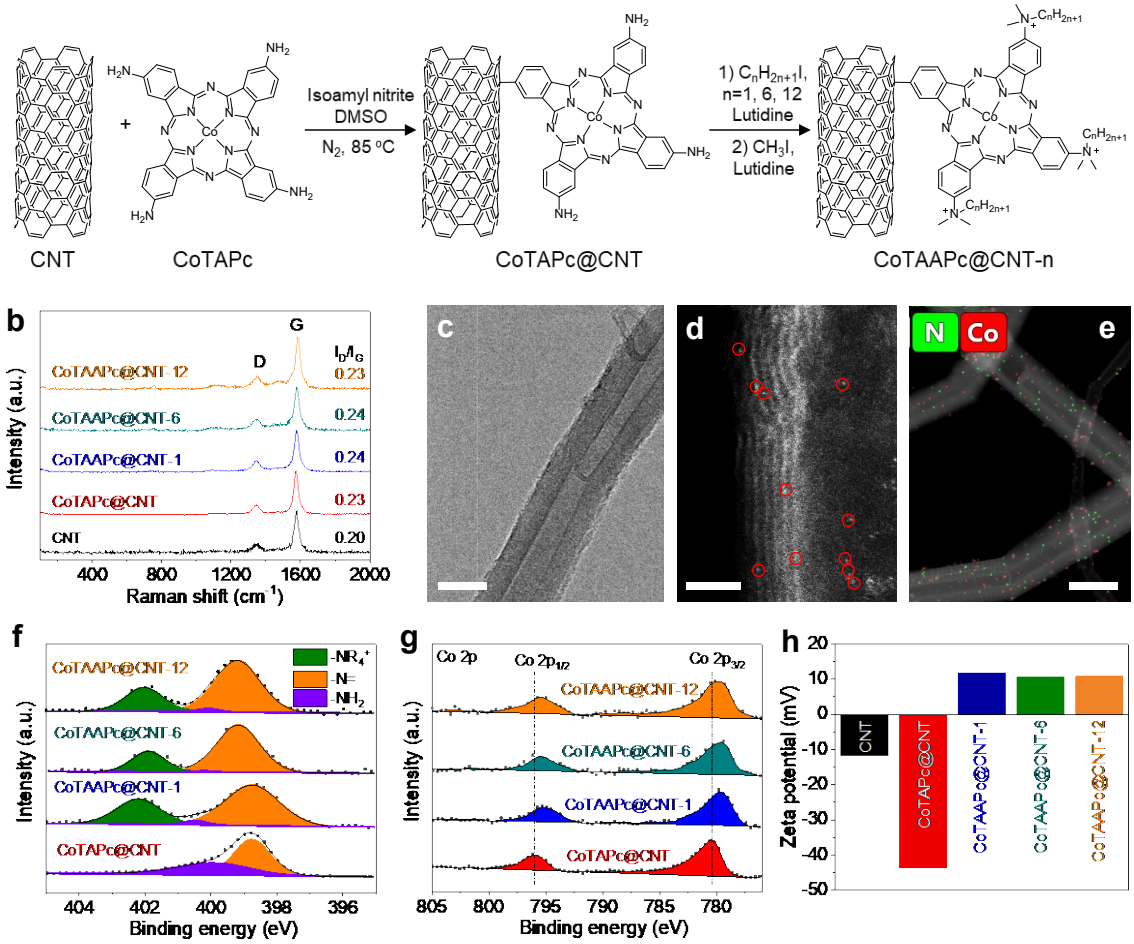

Fig. 2 Synthesis and characterization of CoPc-derived electrocatalysts. a, Scheme for the synthesis of CoTAAPc@CNT-n (n=1, 6, 12). **b**, Raman spectra of pristine CNT, CoTAPc@CNT, CoTAAPc@CNT-1, CoTAAPc@CNT-6 and CoTAAPc@CNT-12. **c**, A typical TEM image of CoTAAPc@CNT-12. **d**, HADDF-STEM of CoTAAPc@CNT-12. The circled bright spots highlight the dispersed Co centers. **e**, N and Co EDS elemental mapping of CoTAAPc@CNT-12. The scale bars are 20 nm, 2 nm, and 25 nm in Fig. 2c, d, and e, respectively. **f**, N 1s XPS spectra of CoTAPc@CNT, CoTAAPc@CNT-1, CoTAAPc@CNT-6 and CoTAAPc@CNT-12. **g**, Co 2p XPS spectra of CoTAPc@CNT,

CoTAAPc@CNT-1, CoTAAPc@CNT-6 and CoTAAPc@CNT-12. **h**, Zeta potential of pristine CNT, CoTAPc@CNT, CoTAAPc@CNT-1, CoTAAPc@CNT-6 and CoTAAPc@CNT-12.

Electrochemical acidic CO_2RR performance

The acidic CO_2 reduction activities of all samples were evaluated in a home-made flow cell in 0.05 M H_2SO_4 + 3.0 M KCl with an electrode area of 1.0 cm^2 (Supplementary Fig. 9). The primary gas products detected are only CO and H_2, with no liquid products generated according to ^{1}H NMR (Supplementary Figs. 10 and 11). As revealed by the polarization curves (Fig. 3a), CoTAAPc@CNT-12 shows slightly higher acidic CO_2RR current density between -0.50 to -1.00 V versus the reversible hydrogen electrode (RHE; all potentials refer to RHE in the remaining discussion). However, the activities start to diverge under more negative potentials. Both CoPc/CNT (physically mixed sample) and CoTAPc@CNT without quaternary ammonium groups have similar acidic CO_2RR activities. Their current densities are the smallest and FE_{CO} quickly declines after -1.2 V, which is similar to a recent report[30]. In comparison, the CoTAAPc@CNT-n catalysts present significantly improved current densities under the same potentials. Specifically, our CoTAAPc@CNT-12 delivers the highest current density of 347.1 mA cm^{-2} at -1.50 V, which is significantly higher than CoTAAPc@CNT-1 (156.7 mA cm^{-2}) and CoTAAPc@CNT-6 (200.0 mA cm^{-2}). Besides the high activity, the CO selectivity of CoTAAPc@CNT-12 is also greatly improved from its counterparts when operating under much more negative potential (Fig. 3b). The CO selectivity of CoTAPc@CNT reaches a maximum of ~100% at 79.7 mA cm^{-2} near -1.34 V, and decreases to only ~70% at -1.62 V, which is attributed to enhanced HER at higher overpotential. In sharp contrast, our CoTAAPc@CNT-12 delivers a ~100% CO selectivity at 140.0 mA cm^{-2}, and maintains a 93.3% selectivity at 609.7 mA cm^{-2}, which corresponds to a CO partial current of 568.6 mA cm^{-2} (Fig. 3c). The density of Co atoms in CoTAAPc@CNT-12 is almost the same as that of other samples, which excludes the possibility that the improved activity originates from a higher density of active sites. The impact of both long alkyl chains and quaternary ammonium cations was further revealed when we calculated the turnover frequency (TOF) of our five cobalt phthalocyanine-derived electrocatalysts by normalizing the acidic CO_2RR activity to the number of Co atomic sites according to ICP results (Supplementary Fig. 12). The TOF values of the five samples are quite similar within the -0.50 to -1.00 V region, again confirming their similar Co active sites. However, in the higher overpotential region, our CoTAAPc@CNT-12 (27.56 s^{-1}) shows an

improvement of up to fivefold compared to the CoTAPc@CNT (5.07 s^{-1}). It is clear that the low TOF value of our CoTAPc@CNT is mainly due to the limited HER suppression in acidic environment at high overpotential. Therefore, these acidic CO_2RR results support our hypothesis that introduction of long alkyl chains and quaternary ammonium cations into the molecular catalysts is important and adequate for suppressing HER in acidic media, delivering an industrially relevant current density with remarkable CO selectivity. With excellent ability to inhibit HER, the CO_2-to-CO performance of our CoTAAPc@CNT-12 is among the best compared to previous reports, including noble metal catalysts[16,25,26,55,56], metal porphyrins/phthalocyanines[57,58], single atom catalysts and non-noble metal-based catalysts (Supplementary Table 1)[23,28,43,58-62].

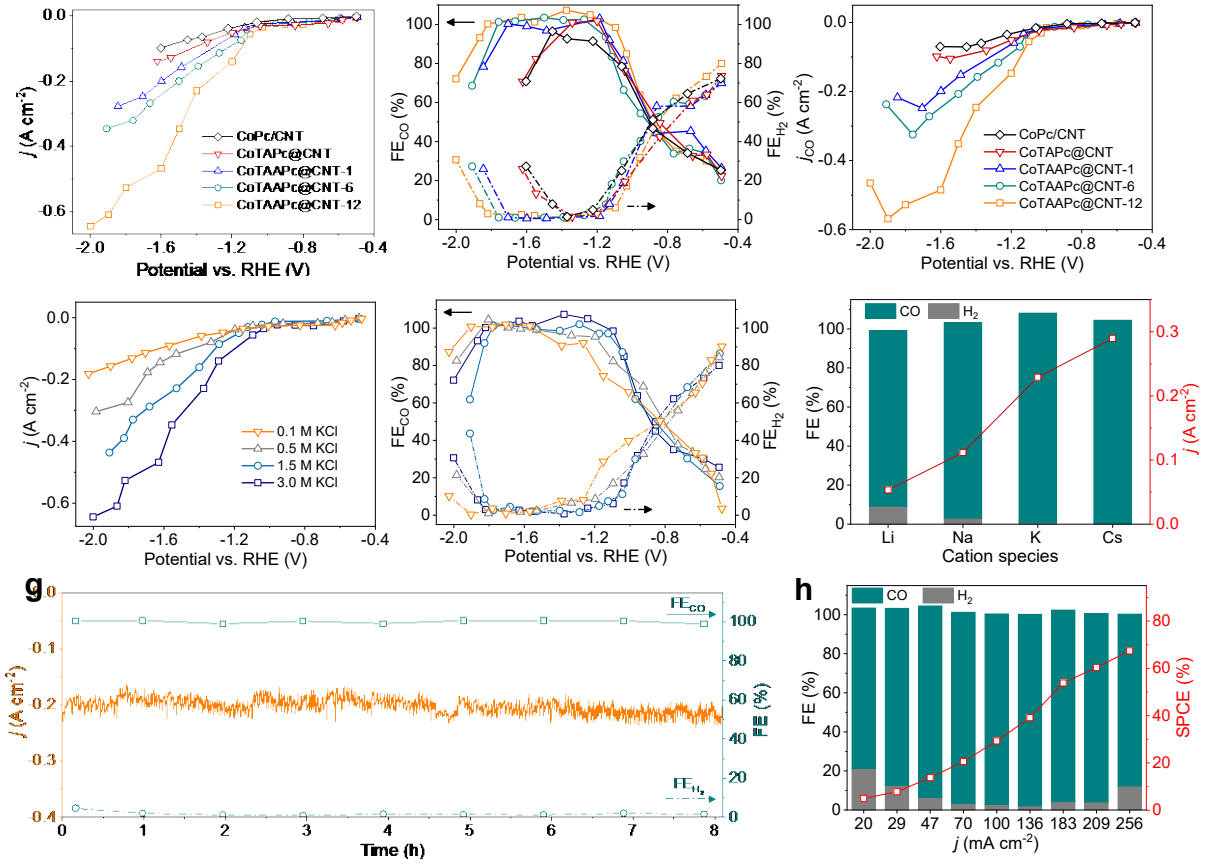

Fig. 3 Acidic electrochemical CO_2RR performance of CoPc-derived electrocatalysts in flow cell. a, Total current density curves. **b**, Faradaic efficiency measurements. **c**, Carbon monoxide partial current density curves of CoPc/CNT, CoTAPc@CNT, CoTAAPc@CNT-1, CoTAAPc@CNT-6 and CoTAAPc@CNT-12 in 0.05 M H_2SO_4 + 3.0 M KCl. **d**, Total current density curves. **e**, Faradaic efficiency measurements of CoTAAPc@CNT-12 in 0.05 M H_2SO_4 with various K^+ concentrations. **f**, Faradaic efficiency and total current density for CoTAAPc@CNT-12 in 0.05 M H_2SO_4 + 3.0 M MCl (Li,

Na, K, Cs) at -1.37 V vs. RHE. **g**, Total current density and H_2, CO FE of acidic CO_2RR during long-term stability test on CoTAAPc@CNT-12 at around 200 mA cm^{-2}. The final CO FE is above 98.0%. **h**, SPCE and FE of H_2 and CO on CoTAAPc@CNT-12 at different total current densities with a CO_2 gas flow rate of 10 sccm.

In previous studies of acidic CO_2RR, high alkali cation concentration was commonly employed to suppress HER because their catalysts showed a lower CO_2RR FE at low concentrations. This was observed for the Ni-N-C catalyst, which showed a lower FE to CO at a K^+ concentration of 0.2 M[62]. However, achieving boosted CO_2RR with lower alkali cation concentration will be beneficial for avoiding salt precipitation during electrolysis. Here, the acidic CO_2 electrolysis was further conducted in 0.05 M H_2SO_4 with various K^+ concentrations (Fig. 3d, e). Surprisingly, in a low K^+ concentration of 0.1 M, our CoTAAPc@CNT-12 demonstrates ~100% FE_{CO} from 90 to 160 mA cm^{-2} over a wide potential window up to -1.8 V. We attribute this high selectivity partially to the long alkyl chains and to the quaternary ammonium cations, which suppress competing HER. With increasing K^+ concentrations in acidic electrolyte, the total current density dramatically increases at the same applied potential. We also compared the performance of CoTAAPc@CNT-12 for CO_2 electroreduction in acidic (0.05 M H_2SO_4 + 3.0 M KCl), neutral (3.0 M KCl), and alkaline (3.0 M KOH) media (Supplementary Fig. 13). As expected, the total current density was largest in an alkaline medium at the same potential. CoTAAPc@CNT-12 maintains a high selectivity of >90% over a wide potential range from -0.45 to -1.34 V but decreases to 85.6% at -1.42 V. In neutral media, a larger potential is needed to achieve the same current density because of the higher ohmic resistance (Supplementary Fig. 14). The highest CO partial current density of 327.7 mA cm^{-2} is achieved at -1.80 V but with a lower selectivity of 82.3%. While in acidic media, our CoTAAPc@CNT-12 shows high-yield production of CO, attaining a much higher FE_{CO} of ~100% and a large partial current density of 526.8 mA cm^{-2} at -1.82 V.

We next probed whether other alkali cations, such as Na^+, Cs^+, and especially Li^+, would influence the competition between HER and CO_2RR (Fig. 3f). In most studies, HER cannot be effectively suppressed in Li^+ electrolytes such that the CO_2RR selectivity is often poor (Supplementary Table 2)[16,19,25,26,63-66]. In stark contrast, our CoTAAPc@CNT-12 could promote acidic CO_2 reduction (FE_{CO}>90%) with all types of alkali cations. The Faradaic efficiencies for H_2 increase in the order of

Cs≈K<Na<Li, while the H_2 partial current densities also increase in a similar order of Cs<K<Na<Li (Supplementary Fig. 15).

We further evaluated the long-term stability of CoTAAPc@CNT-12 in a flow cell at -1.35 V in 0.05 M H_2SO_4 + 3.0 M KCl. The total current density was maintained at ≈200 mA cm^{-2} for 8 h, while the CO selectivity remained >98% throughout the test (Fig. 3g). The characterizations based on post-reaction analysis collectively demonstrate excellent maintenance of the CoTAAPc@CNT-12 catalyst after long-term electrolysis with negligible catalyst leaching, in accordance with the maintained catalytic performance (Supplementary Fig. 16). For example, no obvious change is observed in the UV-vis spectroscopy, Co 2p of XPS data, nor the Raman. After 8 h of electrolysis at ≈200 mA cm^{-2}, negligible Co content was detected in the electrolytes during ICP tests (Supplementary Table 3). On the other hand, the pH in the catholyte and anolyte remained almost unchanged after acidic CO_2RR catalysis (Supplementary Fig. 17). Such a stable electrolyte environment can also contribute to the catalytic stability of CoTAAPc@CNT-12 in acid. However, the catholyte pH of CO_2RR in KOH media decreases from 13.92 to 8.77 during the electrochemical process, probably due to the reaction of OH^- with CO_2. Great long-term stability of CoTAAPc@CNT-12 at a lower K^+ concentration was also achieved (Supplementary Fig. 18).

We also explored the effectiveness of polymer coating on molecular electrocatalysis using polytetrafluoroethylene (PTFE), which has been shown to alleviate flooding and suppress HER in wide potential windows[43]. However, our experimental results reveal that the addition of PTFE does not significantly increase the operating potential window compared to our covalently grafted molecular catalyst (Supplementary Fig. 19). Moreover, the high impedance of PTFE leads to a decreased current density.

As mentioned above, acidic CO_2RR can suppress (bi)carbonate formation to improve carbon efficiency. Thus, we further examined the SPCE of acidic CO_2RR at 10 sccm of CO_2 flow rate in a home-made flow cell with a larger electrode area of 4.0 cm^2 (Fig. 3h). By gradually increasing the current density from 20 to 256 mA cm^{-2}, the SPCE reaches a high value of 67.4% for CO production in the acidic system. When the CO_2 flow rate is decreased from 10 to 1 sccm, we achieve a remarkable SPCE of 84% for the totality of CO_2RR product: 84% of CO_2 introduced at the inlet was converted to CO at the outlet (Supplementary Fig. 20). Overall, the demonstrated higher SPCE of the acidic CO_2RR is due to inhibition of carbonate formation. Moreover, our SPCE also exceeds most reported values in other alkaline or acidic

systems[16,19,25,26,28,29,41,56,67-72], validating the superiority of our design (Supplementary Table 4).

Electrochemical mechanism studies on inhibiting HER

The above experimental results clearly suggest that quaternary ammonium cations with long alkyl chains can suppress competing HER and simultaneously promote CO production in strongly acidic electrolytes. To shed light on the roles of alkyl chains and quaternary ammonium cations in suppressing HER, we measured the polarization curves of a rotating-disk electrode coated with different catalysts in 0.05 M H_2SO_4 + 0.5 M K_2SO_4 (Fig. 4a and Supplementary Fig. 21). The polarization curves at 1600 rpm are summarized in Fig. 4b. The onset potentials of HER for CoTAAPc@CNT-n and CoPc/CNT are close to each other. On all electrodes, a current density plateau was observed, which corresponds to HER from diffusion-limiting hydronium reduction. Compared to CoTAPc@CNT, CoTAAPc@CNT-12 shows a smaller plateau current density (Fig. 4b), presumably due to attenuated H_3O^+ mass transfer to the cathode surface. The linear fit of the plateau current ($j_{plateau}$) using the Levich equation (Supplementary Fig. 22 and Supplementary Table 5) suggests a ~10% decrease in the H_3O^+ diffusion coefficient ($D_{H_3O^+}$) for CoTAAPc@CNT-12 versus CoTAPc@CNT. We further calculated the kinetic current densities using the Koutecký-Levich equations, showing a 10-fold decrease in HER current density from 1141 mA cm^{-2} to 141 mA cm^{-2} for CoTAPc@CNT and CoTAAPc@CNT-12, respectively. In addition, for CoTAPc@CNT, the current density increases again at ~ -1.20 V, where reduction of water starts. In stark contrast, water reduction starts at -1.60 V for CoTAAPc@CNT-12. CoTAAPc@CNT-12 showed significantly diminished H_2O reduction current density at more negative potential compared with CoTAPc@CNT. The water reduction activities decrease in the same order of CoTAAPc@CNT-12 < CoTAAPc@CNT-6 < CoTAAPc@CNT-1 < CoTAPc@CNT ≈ CoPc/CNT. We also measured the water contact angles (Supplementary Fig.23). All samples are hydrophobic with water contact angles >90°. Due to its ionic nature, the water contact angle of CoTAAPc@CNT-1 is slightly smaller than CoTAPc@CNT. As the alkyl chains become longer, the hydrophobicity increases with water contact angles of 124° and 130° for CoTAAPc@CNT-6 and CoTAAPc@CNT-12, respectively. Therefore, the rotating-disk electrode experiments show that the hydrophobic and cationic interface microenvironments generated by the quaternary ammonium cations reduce the activity of hydronium and water reduction, thus improving acidic

CO_2 electroreduction. Moreover, the LSV curves of GDL in a flow cell under Ar-statured acidic electrolyte further confirm our analysis (Supplementary Fig. 24). We also tested with a graphite rod to exclude the potential interference of the counter electrode, which caused negligible influence on our RDE experiments (Supplementary Fig. 21d, e)[73,74].

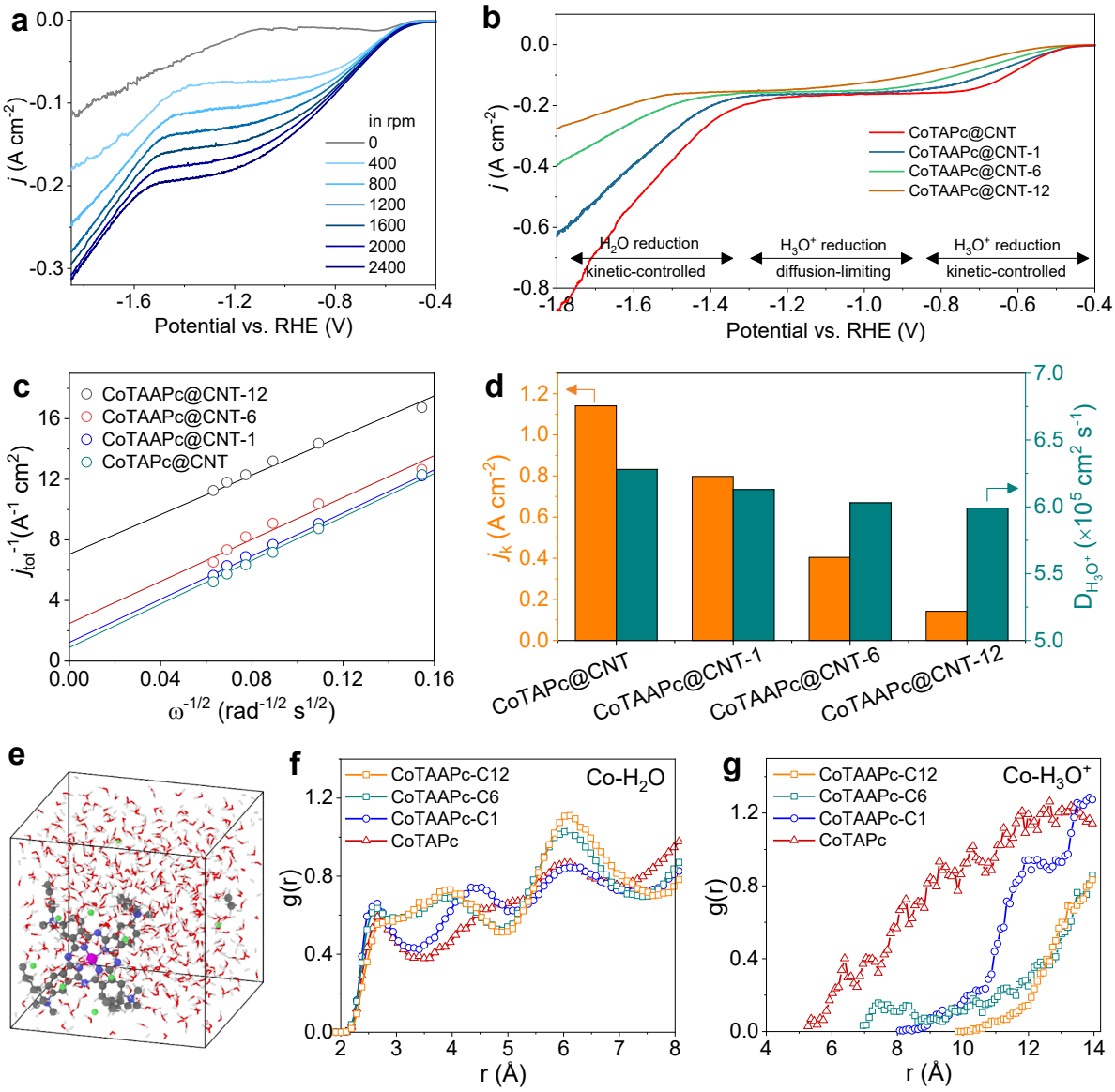

Fig. 4 Mechanistic studies. a, LSV curves of CoTAAPc@CNT-12 in N_2-saturated electrolyte of 0.05 M H_2SO_4 and 0.5 M K_2SO_4 under varied rotating speed and **b**, comparison of different samples at 1600 rpm. **c**, Koutecký-Levich plot of different samples at -0.8 V. **d**, Kinetic current density of HER and diffusion coefficient of hydronium calculated from Koutecký-Levich equations. **e**, A typical model of CoTAAPc@CNT-6 for MD simulations. **f**, Radial distribution functions (g(r)) of H_2O surrounding the Co centers for varying alkyl chain lengths and **g**, g(r) of H_3O^+ for different alkyl chains.

To simulate the microenvironments surrounding our catalysts, we utilized molecular dynamics (MD) simulations. See the Computational Methods section for more details on the MD simulations. We previously utilized MD simulations to understand how organic thin films deposited on Cu catalysts can steer the selectivity of CO_2RR[75]. We specifically investigated how the transport of H_2O and CO_2 changes in different hydrophobic environments and with varying concentration of charged species (namely K^+). In the present case, we are particularly interested in the distribution of H_2O and H_3O^+ relative to the Co catalyst centers. We expect that the cationic ammoniums installed on the perimeters of the catalysts should repel other cationic species. Since H_3O^+ is expected to reside far from the catalyst, this would shut down HER.

To quantitively evaluate the distributions of species surrounding the solvated catalysts, we first computed radial distribution functions, g(r), displaying the distribution of H_2O surrounding the central Co catalysts (Fig. 4f). The distribution of H_2O surrounding Co in CoTAAPc@CNT-1 has its first peak at ~2.7 Å and its second peak at ~4.5 Å, representing the first and second solvation shells, respectively. That g(r) clearly dips between these two peaks, indicating two discrete solvation shells. CoTAAPc@CNT-6 also exhibits a first peak at ~2.7 Å. However, the second g(r) peak, representing the second solvation shell, is located at ~3.8 Å. Moreover, g(r) exhibits less of a dip between these two peaks, suggesting a more continuous distribution of H_2O between the two solvation shells. We consider that that this modulation of the second solvation shell is due to the alkyl chains disrupting the hydrogen bonding network of H_2O surrounding Co. This claim is further substantiated from the H_2O distribution encompassing CoTAAPc@CNT-12. The H_2O around CoTAAPc@CNT-12 exhibits no peak at ~2.7 Å; instead, the first peak is that of the disrupted second solvation shell at ~3.9 Å. This lack of a first solvation shell peak and the gradual redistribution of H_2O from 2.5 to 3.9 Å suggest that the C_{12} alkyl chains completely inhibit ordered packing of water near Co. The cationic ammoniums repel H_3O^+ from the catalyst to suppress HER. The alkyl chains disrupt hydrogen bonding of water near the catalyst which plays two roles. First, the broken hydrogen bonding produces a more hydrophobic environment, which allows CO_2 to reside near the catalytic site and be reduced more readily. Second, the broken hydrogen bonding inhibits proton jumping from H_3O^+ to the catalyst *via* the Grotthuss mechanism, further suppressing HER.

We also analyzed the distribution of H_3O^+ near the Co center (Fig. 4g). It appears that the H_3O^+ tends

to reside beyond 7 Å from the Co center, likely due to coulombic repulsion with the positively charged alkylammoniums present on the molecules. The general trend suggests that H_3O^+ are more likely to reside < 14 Å from the Co center for CoTAAPc@CNT-1, followed by CoTAAPc@CNT-6, and then CoTAAPc@CNT-12. We note that during the CoTAAPc@CNT-6 simulation, one H_3O^+ spent significant time at 7-9 Å from the Co center. We found this to be a result of how the simulation was initialized; specifically, this particular H_3O^+ randomly spawned near a Cl^- in one of the simulations. The close proximity of H_3O^+ to the Cl^- stabilized the H_3O^+ closer to the Co center, resulting in the non-negligible population of H_3O^+ 7-9 Å from the Co for CoTAAPc@CNT-6. Aside from this anomaly, the distribution of H_3O^+ for the three catalysts indicates that longer alkyl chains force H_3O^+ to reside further from the Co center. Combining all our analyses together, the acidic CO_2RR performance on CoTAAPc@CNT-12 catalyst can be convincingly ascribed to the advantageous synergies between quaternary ammonium cation and the long alkyl chain in optimizing the microenvironment near the catalyst surface, which greatly reduces H_3O^+ and H_2O coverage to suppress competing HER while promoting the CO_2 reduction process. Our MD simulations agrees well with these RDE results. In addition to the electric field effect, the longer alkyl chains also introduce an aerophilic-hydrophobic microenvironment at the catalyst-electrolyte interface, which increases the interfacial gas availability and further improves CO_2RR[76].

The versatility of quaternization strategy

We further demonstrated the easy adaptation of our strategy towards a wide range of molecular catalysts (NiTAAPc@CNT-12, SnTAAP@CNT-12 and CuTAAPc@CNT-12) for acidic CO_2RR. The successful synthesis can be inferred from FT-IR, XPS, and zeta potential analysis (Supplementary Figs. 25-27), showing similar trends to those of CoPc-based catalysts. We also explored the effect of quaternary ammonium cations with long alkyl chains in comparison to their counterparts without functionalization (Fig. 5a-f).

NiTAPc is another molecular catalyst that is selective for CO production. Upon introducing the quaternary ammonium groups with long alkyl chains, HER was suppressed dramatically (Fig. 5a, b). Thus, the H_2 FE at ~ -1.67 V dropped from 54.9% for NiTAPc@CNT to 0.4% for NiTAAPc@CNT-12. The partial current density of CO also increased from 51.3 to 210.1 mA cm^{-2} (Fig. 5b). We also evaluated iron porphyrin and phthalocyanine molecules, which also produce CO as the major product (Supplementary

Figs. 28 and 29)[77,78]. Although FeTAAP@CNT-12 shows higher CO selectivity than FeTAP@CNT, the maximum FE_{CO} achieved is 50% due to demetallation during CO_2RR.

SnTAP@CNT and SnTAAP@CNT-12 mainly catalyze CO_2-to-HCOOH (Fig. 5c, d). Due to its strong HER inhibition at high overpotential, our SnTAAP@CNT-12 showed a surprisingly wide potential window for HCOOH production, ranging from -1.39 to -1.86 V with FE_{HCOOH} >70%. However, SnTAP@CNT only works from -1.42 to -1.58 V for FE_{HCOOH} >70%. To confirm that formic acid is derived from CO_2 rather than from other impurities, isotopic-labelling experiments were conducted using SnTAAPc@CNT-12 under continuous $^{13}CO_2$ flow. The ^{1}H NMR peak splitting at 8.24 ppm verifies that the formic acid produced originates from the CO_2 input (Supplementary Fig. 30).

Both CuTAPc@CNT and CuTAAPc@CNT-12 can reduce CO_2. Although in-situ generation of copper nanoparticles may occur[79], we still observe enhanced acidic CO_2RR, possibly due to the near-surface microenvironment induced by the quaternary ammonium groups. The highest methane FE achieved on CuTAPc@CNT is only 5.1% at -2.01 V, which significantly improves to 41.7% on CuTAAPc@CNT-12 (Fig. 5e, f and Supplementary Fig. 31). The TOF values are summarized in Supplementary Fig. 32, further highlighting the improved performance in acidic medium with modifications. Overall, after introducing quaternary ammonium groups with long alkyl chains to the molecular catalysts, all samples show higher current density and product turnover frequency in acidic CO_2RR performance than their counterparts, due to favorable HER suppression.

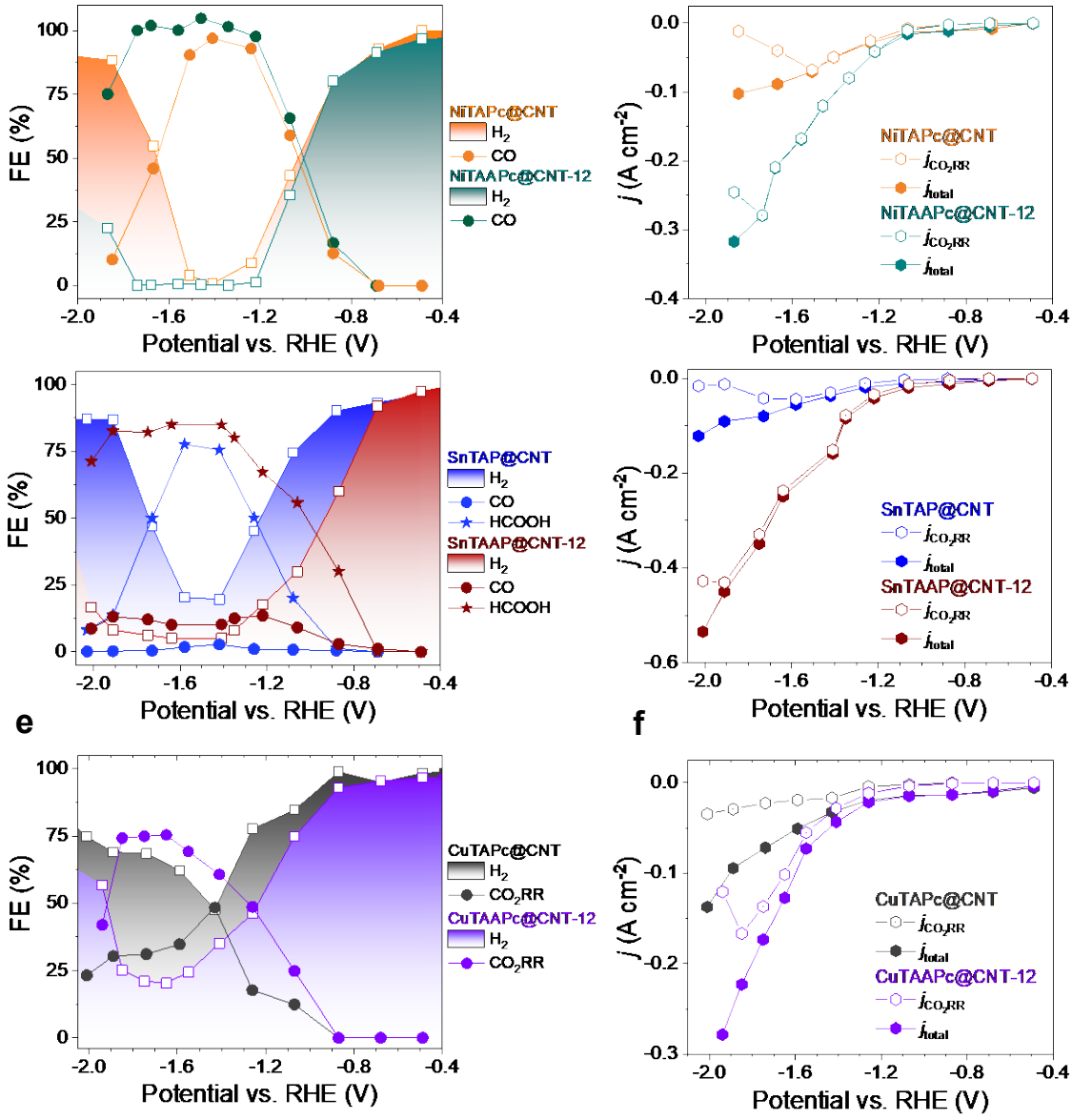

Fig. 5 Performance of acidic CO_2 reduction on extended electrocatalysts in a flow cell set-up. Faradaic efficiency and current density in 0.05 M H_2SO_4 + 3.0 M KCl at different applied voltages. The catalysts used were NiTAPc@CNT and NiTAAPc@CNT-12 (**a**, **b**), SnTAP@CNT and SnTAAP@CNT-12 (**c**, **d**), CuTAPc@CNT and CuTAAPc@CNT-12 (**e**, **f**).

Conclusion

We have developed a general chemical strategy for synthesizing covalently grafted molecular catalysts with quaternary ammonium cations and long alkyl chains. We subsequently synthesized a family of

M@CNT-12 (M=CoTAAPc, NiTAAPc, CuTAAPc and SnTAAP). Most importantly, the covalently grafted molecular catalysts can be functionalized peripherally with quaternary ammonium groups, which form hydrophobic-aerophilic interface microenvironments that play dominant roles in delivering industrially relevant reaction rates. The ability of this method to introduce quaternary ammonium groups with long alkyl chains enables us to obtain a superior electrocatalyst (CoTAAPc@CNT-12), which exhibits an excellent FE_{CO} at an industrially relevant current for acidic CO_2RR. Our CoTAAPc@CNT-12 shows highly selective CO_2RR with a FE_{CO} of >93% over a surprisingly wide range of current densities from 56.2 to 609.7 mA cm^{-2} in strong acid (pH<1), achieving an unprecedented CO partial current density of 568.6 mA cm^{-2}. Due to the inhibition of carbonate formation in acid, an extremely high SPCE of 60.4% is also reached for CO production together with excellent selectivity of 96.4% and current density of >200 mA cm^{-2}, exceeding the value in alkaline CO_2 electrolysis. Our mechanistic studies provide insights into how the cation effect and the alkyl effect suppress HER and boost CO_2RR production. On one hand, these cationic groups repulse the hydronium for HER while electrostatically stabilizing the negatively charged CO_2^- intermediate[38]. On the other hand, the long alkyl chains regulate the interfacial water environment by repelling isolated water and thus suppressing HER. CO_2 reduction is simultaneously promoted since the alkyl chains provide multiple aerophilic tunnels for CO_2 transportation. Beyond a promising catalytic system for efficient acidic CO_2RR, we believe the developed synthesis method is universal for various catalysts and will allow molecular catalysts to be adopted for practical applications in the fields of catalysis and energy.

Methods

Materials

All reagents and chemicals were obtained from commercial sources and used as received without any further treatment. Cobalt phthalocyanine (CoPc, 92%), isoamyl nitrite, dimethyl sulfoxide (DMSO), iodomethane (CH_3I), 1-iodohexane($C_6H_{13}I$), 1-iodododecane($C_{12}H_{25}I$) and 2,6-lutidine (99%) were purchased from J&K Chemical Ltd. Cobalt(II) tetraamino phthalocyanine (CoTAPc, 95%), copper(II) tetraamino phthalocyanine (CuTAPc, 95%) and nickel(II) tetraamino phthalocyanine (NiTAPc, 95%) were purchased from Shanghai Kylpharm Co., Ltd. 5,10,15,20-tetrakis(4-aminophenyl)-porphinatotin (SnTAP, 95%) were obtained from Shanghai Tensus biotech. Co., Ltd. Multi-walled carbon nanotubes (MWCNTs, OD: 10-20 nm, L: 5-30 μm) were bought from XFNANO. Ethanol, diethyl ether and N, N-

Dimethylformamide (DMF) were supplied by AQA, USA. Anion exchange membrane (FAB-PK-130, FuMA-Tech), Nafion (SigmaAldrich), proton exchange membrane (Nafion 117, Fuel Cell Store), gas diffusion layer (28BC, SGL Carbon Sigracet) and were purchased from the corresponding reagent company. Deionized water (Millipore Milli-Q grade) with a resistivity of 18.2 MΩ/cm was used in all experiments.

Catalyst Synthesis

Synthesis of CoTAAPc@CNT with different alkyl chain lengths. Typically, 30 mg CNTs and 34.5 mg CoTAPc were added into 10 mL DMSO solution and sonicated for 10 min. 7.5 μL isoamyl nitrite was dropwise added to the above solution with vigorous stirring. Then the mixture was heated at 85°C for 24 h in N_2 atmosphere. When the system was cooled down, the product was collected via centrifugation at 4500 rpm for 15 min and washed with DMF (20 mL × 3 times) and DI water (20 mL × 3 times) until the solvent become colourless to remove residues. The product then was vacuum dried at 60°C overnight to give CoTAPc@CNT composite, bottled and stored in refrigerator for later use. Next, 30 mg CoTAPc@CNT and 5 mL DMF were added into a 20 mL round bottom flask. The mixture was sonicated for 10 min and then 1 mL 2,6-lutidine and 16 mmol iodoalkane (that is 1 mL iodomethane, 2.5 mL 1-iodohexane or 4.0 mL 1-iodododecane) were added. The mixture was stirred at 80°C for 12 h in N_2 atmosphere and obtained product was collected by centrifugation, washed with DMF and DI water and vacuum dried for later use. Finally, 30 mg product prepared above was dispersed in 5 mL DMF. 1 mL 2,6-lutidine and 1 mL iodomethane were added, heated at 70°C for 24 h in N_2 atmosphere. After reaction, the product was centrifuged and repeatedly washed with DMF and DI water and evacuated at 60°C overnight to yield CoTAAPc@CNT-1, CoTAAPc@CNT-6 and CoTAAPc@CNT-12, respectively.

Synthesis of various M@CNT-12. The synthesis method of various M@CNT-12 is same as that of CoTAAPc@CNT-12. However, 35.0 mg CuTAPc, 34.7 mg NiTAPc and 43.53 mg SnTAP were used for preparing CuTAAPc@CNT-12, NiTAAPc@CNT-12 and SnTAAP@CNT-12, respectively.

Characterization

Fourier transform infrared (FT-IR) spectroscopy was measured using KBr pellets on a Perkin Elmer Spectrum 100 spectrometer in the 400-4000 cm^{-1}. Raman spectroscopy was collected using a LabRAM HR800 laser confocal micro-Raman spectrometer with a laser wavelength of 514.5 nm. The X-ray photoelectron spectroscopy (XPS) was obtained on a Thermo ESCALAB 250Xi spectrometer equipped

with an Al Kα radiation source (1486.6 eV, pass energy 20.0 eV). The binding energy was corrected by the C 1s peak at 284.8 eV. UV-vis spectrophotometry was performed on a Shimadzu 1700 spectrophotometer in DMF solution with a concentration of 1×10^{-5} mol mL^{-1}. Zeta-potential was determined on a dynamic light scattering particle size analyser (Malvern Zetasizer Nano-ZS). Samples were dispersed in DI water and sonicated for 1 h before the test. ^{1}H NMR spectra were recorded on a Bruker 600 MHz ASCEND AVANCE III HD Nuclear Magnetic Resonance System. Scanning transmission electron microscopy was characterized on a double spherical-aberration-corrected FEI Themis Z microscope at 60 kV. Transmission electron microscopy (TEM) was carried out on a Philips Technai 12 with an accelerating voltage of 120 kV and a JEM-2100F high-resolution TEM (HRTEM) equipped with EDS detector at an accelerating voltage of 200 kV. Inductively coupled plasma optical emission spectroscopy (ICP-OES) measurements were conducted on an Optima 8000 spectrometer. The sample was subjected to concentrated HNO_3 and heated at 90°C for half an hour. After that, the mixture was diluted with DI water and filtered through a filter paper. The filtrate was collected for analysis.

Preparation of working electrodes

Typically, 10 mg covalently grafted catalysts, 4 mL ethanol and 30 μL of Nafion binder solution (Sigma Aldrich, Nafion 117, 5 wt.%) were mixed together and sonicated for 30 min to obtain a homogeneous ink. Then, the well-dispersed ink was dip-coated onto the 1×2.5 cm^2 or 2.5×2.5 cm^2 Sigracet 28 BC gas diffusion layer (Fuel Cell Store) electrodes and subsequently dried naturally overnight to give the desired catalyst loading (1 mg cm^{-2}). The active area of working electrodes during the test was 1 cm^2 or 4 cm^2. For the preparation of the physically mixed sample, CoPc/CNT, 0.6 mg CoPc, 9.4 mg CNT and 30 μL Nafion were dissolved in 4 mL ethanol and sonicated for 30 min. Then 1 mL catalyst ink was dropped on the 1×2.5 cm^2 gas diffusion layer and dried naturally overnight. For another physically mixed sample, CoPc/CNT-50% PTFE, a PTFE mass ratio of 50% (5 mg) was added to the CoPc/CNT catalyst ink.

Electrochemical measurements

The acidic CO_2RR performance was evaluated in a three-electrode system in a flow cell assembly. The area of the electrode exposed was 0.5×2.0 cm^2 or 2.0×2.0 cm^2. The used flow cell assembly consists of gas flow chamber, anolyte chamber and catholyte chamber. Each chamber contains an inlet and outlet for gas or electrolyte. The anolyte chamber was separated from the catholyte chamber by a Nafion 117 cation exchange membrane (Fuel Cell Store). 40 mL of 0.05 M H_2SO_4 containing various concentrations of KCl

(0.1/0.5/1.5/3.0 M) was used as catholyte. Their pH values were 0.94, 0.81, 0.65 and 0.52, respectively, detected by a pH meter (PHS-3E). And 40 mL of 0.10 M H_2SO_4 containing 0.5 M K_2SO_4 was used as anolyte. Prior to the electrochemical test, the electrolytes were separately circulated in both the catholyte and anolyte chambers using peristaltic pumps (Longer, BT100-2J) at flow rates of 5 mL min^{-1} and 25 mL min^{-1}, respectively. High purity CO_2 (Linde, 99.999%) gas was continuously supplied to the gas chamber at a rate of 10 sccm (or 1/3 sccm) using a mass flow controller. GDE coated catalysts, Ag/AgCl (3.5 M KCl) electrode equipped with a salt bridge and platinum foil were employed as the working reference and counter electrode, respectively. All potentials were measured against the Ag/AgCl reference electrode and converted to the reversible hydrogen electrode (RHE) reference scale by using the Nernst function with *iR* compensation as below: $E_{vs.\ RHE}=E_{vs.\ Ag/AgCl} + 0.22 + 0.0592\times pH - 0.85\times iR$. CHI650 potentiostat was used to record the electrochemical response. The resistance between the reference electrode and the working electrode was measured by potentiometric electrochemical impedance spectroscopy (PEIS), which was investigated by applying an open circuit voltage in a frequency range from 100 kHz to 0.1 Hz with an amplitude of 5 mV, and manually compensated for 85%. The linear sweep voltammetry (LSV) experiments were scanned in acidic electrolytes with a scan rate of 50 mV s^{-1}. The stability measurements of CO_2RR under acidic electrolytes were performed at potentiostatic conditions (-1.36 V_{RHE}) to record the current density and faradaic efficiency of CoTAAPc@CNT-12 within 8 h.

CO_2RR product analysis

Unless otherwise stated, CO_2 gas was led into gas chamber of flow cell at ambient pressure and room temperature, and then injected into a gas chromatograph (Ruimin GC 2060, shanghai) after CO_2RR to analyse gas products. The GC was equipped with a thermal conductivity detector (TCD) for analysing H_2, and a flame ionization detector (TCD) for analysing carbonaceous substances, while calibrated by using standard mixture gas (Linde) before measurements. Each quantitative sampling was performed three times to achieve accurate results. The FE for a given gas product was calculated as below:

$$FE_{gas} = \frac{Q_{gas}}{Q_{total}} \times 100\% = \frac{n_{gas} \times N \times F}{j \times t} \times 100\% = \frac{\frac{P}{RT} \times N \times F}{j} \times v \times 100\%$$

where n_{gas} is the amount of a given gas product (mol); *N* is the number of electrons transferred to form one molecule of gas product. For H_2, CO, methane and ethylene, *N* equals 2, 2, 8 and 12, respectively; *v* is the

mass flow rate of gas (sccm); j is the total current (mA); F is the Faraday constant (96485 C mol^{-1}); P is the atmosphere pressure (101 kPa), T is the temperature (298 K) and R is the molar gas constant (8.314 J mol^{-1} K^{-1}).

On the other hand, liquid products were analysed afterward by a quantitative ^{1}H NMR (Bruker AVANCE III 300 MHz) with water peak suppression, in which 450 μL electrolyte was mixed with 50 μL DMSO (10 mM, the internal standard solution) in D_2O (Sigma Aldrich, 99.9%). The concentration of a given liquid product was elucidated by its ^{1}H NMR peak area relative to the internal standard. The FE of a solution-phase product was calculated according to the equation:

$$FE_{liquid} = \frac{Q_{liquid}}{Q_{total}} \times 100\% = \frac{n_{liquid} \times N \times F}{j \times t} \times 100\%$$

where n_{liquid} is the amount of a given liquid product (mol); N is the number of electrons transferred to form one molecule of liquid product and equals 2, 8, and 12 for formic acid, acetic acid, and ethanol, respectively. j is the total current (mA). t is the record time (s). F is the Faraday constant (96485 C mol^{-1}).

The single pass carbon efficiency (SPCE) of CO_2 towards producing CO was calculated as follows at 25°C, 1 atm:

$$SPCE = \frac{j_{CO}(mA) \times 60(\text{sec}) \times 24.05(L/\text{min})}{N \times F \times v} \times 100\%$$

where j_{CO} means the partial current of CO; N stands for electron transfer and is 2 for CO product; Note that for precisely analysing gas products and determining SPCE at very low CO_2 gas flow rate (1 sccm), the GC standard curve was re-calibrated by using standard mixture gas with higher concentration (tens of thousands ppm).

Rotating disk electrode test

The RDE experiments were run with CHI650 workstation using PINE 636 rotating-disk electrode system (a diameter of 5 mm). Before tests, the electrode was polished using alumina polishing powder (0.05 μm). 50 μL of the catalyst ink described in 'Preparation of working electrodes' was drop-cast on the RDE and dried under N_2 flow as the working electrode. The Ag/AgCl (3.5 M KCl) electrode and platinum wire were used as the reference and counter electrode, respectively. Tests were performed in N_2 saturated 0.05 M H_2SO_4 + 0.5 M K_2SO_4 solution with a scan rate of 10 mV s^{-1} between 1.86 and 0.36 V at the same rotation rate. All potentials were converted to the RHE. Electrolyte resistance was determined by high-

frequency impedance measurements, and *iR* compensation subsequently performed.

MD simulations

All MD simulations used the Universal Force Field (UFF[80]) to describe the covalent interactions (bonds, angles and dihedrals) as well as the van der Waals interactions. Electrostatics were described using the charge equilibration (QEq[81]) approach. For all simulations, catalysts were solvated in 500 water molecules, along with 5 H_3O^+. 9 Cl^- ions were also solvated in order to maintain the systems at neutral charge. The positions of all species were initialized randomly to avoid bias. All systems were simulated via the canonical (NVT) ensemble using a temperature of 298.15 K. Volumes were chosen such that the density of the systems was equal to that of liquid water.

Data availability

All data available from the authors upon reasonable request.

Acknowledgements

This work was supported by the Guangdong Basic and Applied Basic Research Fund (2022A1515011333), the Hong Kong Research Grant Council (11309723), the State Key Laboratory of Marine Pollution (SKLMP/SCRF/0060) and the Shenzhen Science and Technology Program (JCYJ20220818101204009). B.Z.T. acknowledges support from Shenzhen Key Laboratory of Functional Aggregate Materials (ZDSYS20211021111400001), the Science Technology Innovation Commission of Shenzhen Municipality (KQTD20210811090142053, JCYJ20220818103007014), and the Innovation and Technology Commission (ITC-CNERC14SC01). CBM and WAG acknowledge support from the Liquid Sunlight Alliance, which is supported by the U.S. Department of Energy, Office of Science, Office of Basic Energy Sciences, Fuels from Sunlight Hub under Award Number DE-SC0021266.

Author contributions

R.Y. conceptualized the project. R.Y, B.Z.T. and WAG supervised the project. Q.Z. and J.S. developed and performed the catalyst synthesis. Q.Z conducted most experiments, and CBM performed the calculations. Q.Z., J.S., Y.S., L.H., L.C., G.L., Y.L., Y.X., Q.H. and G.Y. carried out the materials characterization. R.Y., Q.Z., C.B.M. and W.A.G. analyzed the data and wrote the manuscript. All authors discussed the results and commented on the manuscript.

Competing interests

The authors declare no competing interests.

References

1. Chu, S., Cui, Y. & Liu, N. The path towards sustainable energy. *Nat. Mater.* **16**, 16-22 (2017).
2. Nitopi, S. et al. Progress and perspectives of electrochemical CO_2 reduction on copper in aqueous electrolyte. *Chem. Rev.* **119**, 7610-7672 (2019).
3. Song, Y. et al. Atomically thin, ionic-covalent organic nanosheets for stable, high-performance carbon dioxide electroreduction. *Adv. Mater.* **34**, e2110496 (2022).
4. Guo, W. et al. Transient solid-state laser activation of indium for high-performance reduction of CO_2 to formate. *Small* **18**, e2201311 (2022).
5. Jiao, S., Fu, X., Wang, S. & Zhao, Y. Perfecting electrocatalysts via imperfections: towards the large-scale deployment of water electrolysis technology. *Energy Environ. Sci.* **14**, 1722-1770 (2021).
6. Su, J. et al. Building a stable cationic molecule/electrode interface for highly efficient and durable CO_2 reduction at an industrially relevant current. *Energy Environ. Sci.* **14**, 483-492 (2021).
7. Gao, D., Arán-Ais, R.M., Jeon, H.S. & Roldan Cuenya, B. Rational catalyst and electrolyte design for CO_2 electroreduction towards multicarbon products. *Nat. Catal.* **2**, 198-210 (2019).
8. Niu, Z.-Z., Chi, L.-P., Liu, R., Chen, Z. & Gao, M.-R. Rigorous assessment of CO_2 electroreduction products in a flow cell. *Energy Environ. Sci.* **14**, 4169-4176 (2021).
9. Sa, Y.J., Lee, C.W., Lee, S.Y., Na, J., Lee, U. & Hwang, Y.J. Catalyst-electrolyte interface chemistry for electrochemical CO_2 reduction. *Chem. Soc. Rev.* **49**, 6632-6665 (2020).
10. Liu, S.-Q. et al. Bi_2O_3 nanosheets grown on carbon nanofiber with inherent hydrophobicity for high-performance CO_2 electroreduction in a wide potential window. *ACS Nano* **15**, 17757-17768 (2021).
11. O'Brien, C.P. et al. Single pass CO_2 conversion exceeding 85% in the electrosynthesis of multicarbon products via local CO_2 regeneration. *ACS Energy Lett.* **6**, 2952-2959 (2021).
12. Xu, Y. et al. Self-cleaning CO_2 reduction systems: unsteady electrochemical forcing enables stability. *ACS Energy Lett.* **6**, 809-815 (2021).
13. Larrazábal, G.O. et al. Analysis of mass flows and membrane cross-over in CO_2 reduction at high current densities in an MEA-type electrolyzer. *ACS Appl. Mater. Interfaces* **11**, 41281-41288 (2019).
14. Rabinowitz, J.A. & Kanan, M.W. The future of low-temperature carbon dioxide electrolysis depends on solving one basic problem. *Nat. Commun.* **11**, 5231 (2020).
15. Xie, K., Ozden, A., Miao, R.K., Li, Y., Sinton, D. & Sargent, E.H. Eliminating the need for anodic gas separation in CO_2 electroreduction systems via liquid-to-liquid anodic upgrading. *Nat. Commun.* **13**, 3070 (2022).
16. Gu, J., Liu, S., Ni, W., Ren, W., Haussener, S. & Hu, X. Modulating electric field distribution by alkali cations for CO_2 electroreduction in strongly acidic medium. *Nat. Catal.* **5**, 268-276 (2022).
17. Xia, W. et al. Adjacent copper single atoms promote C-C coupling in electrochemical CO_2 reduction for the efficient conversion of ethanol. *J. Am. Chem. Soc.* **145**, 17253-17264 (2023).
18. Oßkopp, M. et al. Producing formic acid at low pH values by electrochemical CO_2 reduction. *J. CO_2 Util.* **56**, 101823 (2022).
19. Qiao, Y. et al. Engineering the local microenvironment over Bi nanosheets for highly selective

electrocatalytic conversion of CO_2 to HCOOH in Strong Acid. *ACS Catal.* **12**, 2357-2364 (2022).

20. Xie, Y. et al. High carbon utilization in CO_2 reduction to multi-carbon products in acidic media. *Nat. Catal.* **5**, 564-570 (2022).

21. Vennekoetter, J. B., Sengpiel, R. & Wessling, M. Beyond the catalyst: how electrode and reactor design determine the product spectrum during electrochemical CO_2 reduction. *Chem. Eng. J.* **364**, 89-101 (2019).

22. Jiao, K. et al. Designing the next generation of proton-exchange membrane fuel cells. *Nature* **595**, 361-369 (2021).

23. Varela, A.S. et al. pH Effects on the selectivity of the electrocatalytic CO_2 reduction on graphene-embedded Fe–N–C motifs: bridging concepts between molecular homogeneous and solid-state heterogeneous catalysis. *ACS Energy Lett.* **3**, 812-817 (2018).

24. Ringe, S. et al. Double layer charging driven carbon dioxide adsorption limits the rate of electrochemical carbon dioxide reduction on Gold. *Nat. Commun.* **11**, 33 (2020).

25. Monteiro, M.C.O., Philips, M.F., Schouten, K.J.P. & Koper, M.T.M. Efficiency and selectivity of CO_2 reduction to CO on gold gas diffusion electrodes in acidic media. *Nat. Commun.* **12**, 4943 (2021).

26. Pan, B. et al. Close to 90% single-pass conversion efficiency for CO_2 electroreduction in an acid-fed membrane electrode assembly. *ACS Energy Lett.* **7**, 4224-4231 (2022).

27. Li, Z. et al. Electron-rich Bi nanosheets promote $CO_2^{\bullet-}$ formation for high-performance and pH-universal electrocatalytic CO_2 reduction. *Angew. Chem. Int. Ed.* **62**, e202217569 (2023).

28. Liu, Z., Yan, T., Shi, H., Pan, H., Cheng, Y. & Kang, P. Acidic electrocatalytic CO_2 reduction using space-confined nanoreactors. *ACS Appl. Mater. Interfaces* **14**, 7900-7908 (2022).

29. Huang, J.E. et al. CO_2 electrolysis to multicarbon products in strong acid. *Science* **372**, 1074-1078 (2021).

30. Zhong, Y. et al. An artificial electrode/electrolyte interface for CO_2 electroreduction by cation surfactant self-assembly. *Angew. Chem. Int. Ed.* **59**, 19095-19101 (2020).

31. Wan, Q. et al. Boosting the faradaic efficiency for carbon dioxide to monoxide on a phthalocyanine cobalt based gas diffusion electrode to higher than 99% via microstructure regulation of catalyst layer. *Electrochimica Acta* **392**, 139023 (2021).

32. Fan, M. et al. Cationic-group-functionalized electrocatalysts enable stable acidic CO_2 electrolysis. *Nat. Catal.* **6**, 763-772 (2023).

33. Weng, S., Toh, W.L. & Surendranath, Y. Weakly coordinating organic cations are intrinsically capable of supporting CO_2 reduction catalysis. *J. Am. Chem. Soc.* **145**, 16787-16795 (2023).

34. Nam, D. H. et al. Molecular enhancement of heterogeneous CO_2 reduction. *Nat. Mater.* **19**, 266-276 (2020).

35. Ren, S. et al. Molecular electrocatalysts can mediate fast, selective CO_2 reduction in a flow cell. *Science* **365**, 367-369 (2019).

36. Wu, Y., Jiang, Z., Lu, X., Liang, Y. & Wang, H. Domino electroreduction of CO_2 to methanol on a molecular catalyst. *Nature* **575**, 639-642 (2019).

37. Kusama, S., Saito, T., Hashiba, H., Sakai, A. & Yotsuhashi, S. Crystalline copper(II) phthalocyanine catalysts for electrochemical reduction of carbon dioxide in aqueous media. *ACS Catal.* **7**, 8382-8385 (2017).

38. Azcarate, I., Costentin, C., Robert, M. & Savéant, J.-M. Through-space charge interaction substituent effects in molecular catalysis leading to the design of the most efficient catalyst of CO_2-to-CO electrochemical conversion. *J. Am. Chem. Soc.* **138**, 16639-16644 (2016).

39. Nie, W., Tarnopol, D.E. & McCrory, C.C.L. Enhancing a molecular electrocatalyst's activity for CO_2 reduction by simultaneously modulating three substituent effects. *J. Am. Chem. Soc.* **143**, 3764-3778 (2021).

40. Li, J. & Kornienko, N. Electrocatalytic carbon dioxide reduction in acid. *Chem Catal.* **2**, 29-38 (2022).

41. Ma, Z. et al. CO_2 electroreduction to multicarbon products in strongly acidic electrolyte via synergistically modulating the local microenvironment. *Nat. Commun.* **13**, 7596 (2022).

42. Zhao, Y. et al. Conversion of CO_2 to multicarbon products in strong acid by controlling the catalyst microenvironment. *Nat. Synth.* **2**, 403-412 (2023).

43. Sheng, X., Ge, W., Jiang, H. & Li, C. Engineering the Ni-N-C catalyst microenvironment enabling CO_2 electroreduction with nearly 100% CO selectivity in acid. *Adv. Mater.* **34**, 2201295 (2022).

44. Nie, W., Heim, G.P., Watkins, N.B., Agapie, T. & Peters, J.C. Organic additive-derived films on Cu electrodes promote electrochemical CO_2 reduction to C_{2+} products under strongly acidic conditions. *Angew. Chem. Int. Ed.* **62**, e202216102 (2023).

45. Chen, J. et al. Facile synthesis of polymerized cobalt phthalocyanines for highly efficient CO_2 reduction. *Green Chem.* **21**, 6056-6061 (2019).

46. Zhu, M., Chen, J., Guo, R., Xu, J., Fang, X. & Han, Y.-F. Cobalt phthalocyanine coordinated to pyridine-functionalized carbon nanotubes with enhanced CO_2 electroreduction. *Appl. Catal. B: Environ.* **251**, 112-118 (2019).

47. Zhang, X. et al. Delocalized electron effect on single metal sites in ultrathin conjugated microporous polymer nanosheets for boosting CO_2 cycloaddition. *Sci. Adv.* **6**, eaaz4824 (2020).

48. Bhuyan, M.M., Okabe, H., Hidaka, Y. & Hara, K. Pectin-[(3-acrylamidopropyl) trimethylammonium chloride-co-acrylic acid] hydrogel prepared by gamma radiation and selectively silver (Ag) metal adsorption. *J. Appl. Polym. Sci.* **135**, 45906 (2018).

49. Li, N., Lu, W., Pei, K. & Chen, W. Interfacial peroxidase-like catalytic activity of surface-immobilized cobalt phthalocyanine on multiwall carbon nanotubes. *RSC Adv.* **5**, 9374-9380 (2015).

50. Zhang, C. & Zhao, J. Effects of pre-corrosion on the corrosion inhibition performance of three inhibitors on Q235 Steel in CO_2/H_2S saturated brine solution. *Int. J. Electrochem. Sci.* **12**, 9161-9179 (2017).

51. Yang, S., Yu, Y., Dou, M., Zhang, Z. & Wang, F. Edge-functionalized polyphthalocyanine networks with high oxygen reduction reaction activity. *J. Am. Chem. Soc.* **142**, 17524-17530 (2020).

52. Ge, W. et al. Dynamically formed surfactant assembly at the electrified electrode-electrolyte interface boosting CO_2 electroreduction. *J. Am. Chem. Soc.* **144**, 6613-6622 (2022).

53. Asasutjarit, R., Theerachayanan, T., Kewsuwan, P., Veeranodha, S., Fuongfuchat, A. & Ritthidej, G.C. Development and evaluation of diclofenac sodium loaded-N-trimethyl chitosan nanoparticles for ophthalmic use. *AAPS PharmSciTech* **16**, 1013-1024 (2015).

54. Han, N. et al. Supported cobalt polyphthalocyanine for high-performance electrocatalytic CO_2 reduction. *Chem* **3**, 652-664 (2017).

55. Moreno-García, P., Kovács, N., Grozovski, V., Gálvez-Vázquez, M.d.J., Vesztergom, S. & Broekmann, P. Toward CO_2 electroreduction under controlled mass flow conditions: a combined inverted RDE and gas chromatography approach. *Anal. Chem.* **92**, 4301-4308 (2020).

56. Li, X. et al. Confinement of an alkaline environment for electrocatalytic CO_2 reduction in acidic electrolytes. *Chem. Sci.* **14**, 5602-5607 (2023).

57. Shen, J. et al. Electrocatalytic reduction of carbon dioxide to carbon monoxide and methane at an immobilized cobalt protoporphyrin. *Nat. Commun.* **6**, 8177 (2015).

58. Jiang, Z. et al. Molecular catalyst with near 100% selectivity for CO_2 reduction in acidic electrolytes. *Adv. Energy Mater.* **13**, 2203603 (2023).

59. Fujinuma, N., Ikoma, A. & Lofland, S.E. Highly efficient electrochemical CO_2 reduction reaction to CO with one-pot synthesized Co-pyridine-derived catalyst incorporated in a nafion-based membrane electrode assembly. *Adv. Energy Mater.* **10**, 2001645 (2020).

60. Wang, Z., Hou, P., Wang, Y., Xiang, X. & Kang, P. Acidic electrochemical reduction of CO_2 using nickel nitride on multiwalled carbon nanotube as selective catalyst. *ACS Sustainable Chem. Eng.* **7**, 6106-6112 (2019).

61. Fan, Q., Bao, G., Chen, X., Meng, Y., Zhang, S. & Ma, X. Iron nanoparticles tuned to catalyze CO_2 electroreduction in acidic solutions through chemical microenvironment engineering. *ACS Catal.* **12**, 7517-7523 (2022).

62. Li, H. et al. Tailoring acidic microenvironments for carbon-efficient CO_2 electrolysis over a Ni-N-C catalyst in a membrane electrode assembly electrolyzer. *Energy Environ. Sci.* **16**, 1502-1510 (2023).

63. Zhang, Q., Shao, X., Yi, J., Liu, Y. & Zhang, J. An experimental study of electroreduction of CO2 to HCOOH on SnO_2/C in presence of alkali metal cations (Li^+, Na^+, K^+, Rb^+ and Cs^+) and anions (HCO_3^-, Cl^-, Br^- and I^-). *Chin. J. Chem. Eng.* **28**, 2549-2554 (2020).

64. Singh, M.R., Kwon, Y., Lum, Y., Ager, J.W., III & Bell, A.T. Hydrolysis of electrolyte cations enhances the electrochemical reduction of CO_2 over Ag and Cu. *J. Am. Chem. Soc.* **138**, 13006-13012 (2016).

65. Malkani, A.S. et al. Understanding the electric and nonelectric field components of the cation effect on the electrochemical CO reduction reaction. *Sci. Adv.* **6**, eabd2569 (2020).

66. Murata, A. & Hori, Y. Product selectivity affected by cationic species in electrochemical reduction of CO_2 and CO at a Cu electrode. *Bull. Chem. Soc. Jpn.* **64**, 123-127 (1991).

67. Cao, Y. et al. Surface hydroxide promotes CO_2 electrolysis to ethylene in acidic conditions. *Nat. Commun.* **14**, 2387 (2023).

68. Shen, H. et al. Acidic CO_2-to-HCOOH electrolysis with industrial-level current on phase engineered

tin sulfide. *Nat. Commun.* **14**, 2843 (2023).

69. Verma, S. et al. Insights into the low overpotential electroreduction of CO_2 to CO on a supported gold catalyst in an alkaline flow electrolyzer. *ACS Energy Lett.* **3**, 193-198 (2018).

70. Hoang, T.T.H. et al. Nanoporous copper-silver alloys by additive-controlled electrodeposition for the selective electroreduction of CO_2 to ethylene and ethanol. *J. Am. Chem. Soc.* **140**, 5791-5797 (2018).

71. Ma, S., Sadakiyo, M., Luo, R., Heima, M., Yamauchi, M. & Kenis, P.J.A. One-step electrosynthesis of ethylene and ethanol from CO_2 in an alkaline electrolyzer. *J. Power Sources* **301**, 219-228 (2016).

72. Yang, K., Li, M., Subramanian, S., Blommaert, M.A., Smith, W.A. & Burdyny, T. Cation-driven increases of CO_2 utilization in a bipolar membrane electrode assembly for CO_2 electrolysis. *ACS Energy Lett.* **6**, 4291-4298 (2021).

73. Ring, L. et al. From bad electrochemical practices to an environmental and waste reducing approach for the generation of active hydrogen evolving electrodes. *Angew. Chem. Int. Ed.* **58**, 17383-17392 (2019).

74. Jerkiewicz, G. Applicability of platinum as a counter-electrode material in electrocatalysis research. *ACS Catal.* **12**, 2661-2670 (2022).

75. Watkins, N.B. et al. Hydrodynamics change tafel slopes in electrochemical CO_2 reduction on copper. *ACS Energy Lett.* **8**, 2185-2192 (2023).

76. Ohlin, C.A., Dyson, P.J. & Laurenczy, G. Carbon monoxide solubility in ionic liquids: determination, prediction and relevance to hydroformylation. *Chem. Commun.* 1070-1071 (2004).

77. Maurin, A. & Robert, M. Noncovalent immobilization of a molecular iron-based electrocatalyst on carbon electrodes for selective, efficient CO_2-to-CO conversion in water. *J. Am. Chem. Soc.* **138**, 2492-2495 (2016).

78. Torbensen, K. et al. Iron porphyrin allows fast and selective electrocatalytic conversion of CO_2 to CO in a flow cell. *Chem. Eur. J.* **26**, 3034-3038 (2020).

79. Weng, Z. et al. Active sites of copper-complex catalytic materials for electrochemical carbon dioxide reduction. *Nat. Commun.* **9**, 415 (2018).

80. Rappe, A.K., Casewit, C.J., Colwell, K.S., Goddard, W.A., III & Skiff, W.M. UFF, a full periodic table force field for molecular mechanics and molecular dynamics simulations. *J. Am. Chem. Soc.* **114**, 10024-10035 (1992).

81. Rappe, A.K. & Goddard, W.A., III. Charge equilibration for molecular dynamics simulations. *J. Phys. Chem.* **95**, 3358-3363 (1991).